Challenge Journal of Concrete Research Letters

Research Article

Behavior of multi-cell steel columns under impact loading

Kamel Kandil [a], Mostafa El-Shami [a], Ghada Mousa Hekal [a,*], Osama Magdy ElGouhary [a]

[a] *Department of Civil Engineering, Menoufia University, Shebin ElKoum, 6132711 Menofia, Egypt*

ABSTRACT

This study investigates the behavior of multi-cell steel columns (MCCs) under impact loading through both experimental and numerical analysis. Twelve specimens, including single-cell columns (SCC) and four-cell MCC configurations, were tested in empty and concrete-filled conditions. The specimens were categorized into three groups based on a fixed height-to-width ratio (*R*). A nonlinear finite element model was developed using ABAQUS and validated against experimental data. Key parameters, including peak deflection, failure modes, deflection-time relationships, maximum impact forces, energy absorption and the rectangularity ratio effect, were examined to provide insights into impact-resistant structural design. The results demonstrate that the internal partitioning of the column into cells significantly reduces local buckling under impact loading by enhancing the section's local stiffness. In addition, internal partitioning improves energy absorption for empty models. On the other hand, concrete-filled models do not show the same behavior although concrete filling significantly improves resistance to impact forces. The results also provides that increase of the *R* ratio results in an increase in impact force and a decrease in mid-point displacement. For empty single-cell columns, an increase in *R* results in a decrease in energy absorption, which may be due to energy dissipation through local buckling under the falling impactor. These findings contribute to the advancement of impact-resistant column designs for applications in structural and transportation engineering.

ARTICLE INFO

Article history:

Received – February 25, 2025
Revision requested – April 21, 2025
Revision received – May 2, 2025
Accepted – May 12, 2025

Keywords:

Multi-cell columns
Energy absorption
Impact loading
Finite element modeling

Citation: Kandil K, El-Shami M, Hekal GM, ElGouhary OM (2025). Behavior of multi-cell steel columns under impact loading. *Challenge Journal of Concrete Research Letters*, 16(2), 95–114.

1. Introduction

Columns are essential structural elements, and their failure can lead to catastrophic consequences. Among various cross-sectional designs, tubular sections have demonstrated outstanding performance under compression, bending, and torsion. Their superior mechanical properties, combined with an aesthetically appealing shape, have made them widely applicable in structural engineering. Tubular sections are commonly used in buildings, bridges, barriers, offshore structures, and towers, among other applications (Wardenier 2001; Wardenier et al. 2010).

When tubular sections have insufficient wall thickness to support the required loads, filling the hollow section with concrete is a proven method to enhance strength. Several studies have investigated the behavior of concrete-filled tubular columns under compression loading, such as the studies conducted by Campbell (1994), Guler et al. (2013), Chu (2014), Patil and Mohite (2014), Bedage and Shinde (2015), and Kirankumar et al. (2016).

As vertical structural elements, columns are particularly vulnerable to environmental hazards such as impact, wind, and earthquakes. Among these, impact loading generates highly localized pressure, often exceeding the intensity of other hazards. This has driven growing research interest in understanding the behavior of empty and concrete-filled hollow sections under impact loading to develop more resilient design methods. Sean-

* *Corresponding author.* E-mail address: gahda.mousa@sh-eng.menofia.edu.eg (G. M. Hekal)
ISSN: 2548-0928 / DOI: https://doi.org/10.20528/cjcrl.2025.02.005

gatith (1997) presented an extensive experimental program and finite element analysis on FRP composite box beams subjected to impact loads, testing 48 simply supported beams while varying impact velocity, striker mass, span length, and wall thickness. Finite element modeling was performed using LS-DYNA3D. Similarly, Bambach et al. (2008) presented experimental program and finite element analysis of hollow and concrete-filled steel beams subjected to large-mass, low-velocity lateral impacts at mid-span. Yousuf et al. (2010) conducted a comprehensive test program to investigate the impact performance of pre-compressed stainless-steel concrete-filled steel tube (CFST) columns. Their study compared stainless steel column with mild steel column and analyzed the behavior of in-filled tubes under both impact and pre-compressive loads. Al-Thairy (2012) investigated the behavior of axially compressed steel columns under vehicle impact, using ABAQUS/Explicit for numerical modeling, conducting a parametric study, developing a simplified vehicle model, proposing an analytical method for column response, and evaluating design provisions. Yousuf et al. (2012) presented an experimental and numerical investigation on the behaviour of hollow and concrete-filled tubular columns from mild steel subjected to static and impact loading. Experimental and numerical results obtained by ABAQUS/Explicit program were compared. Additionally, the impact response of concrete-filled tubes was compared with that of hollow section tubes. Zhu et al. (2018) investigated the lateral impact resistance of rectangular hollow steel tubes and those partially filled with concrete, demonstrating that concrete effectively mitigates local buckling. Hou et al. (2018) conducted a finite element analysis to evaluate the life-cycle behavior of concrete-filled steel tubes (CFST) subjected to pre-loading, residual stress, and lateral impact. Yang et al. (2019) and Zhu et al. (2023) investigated the impact force, deformation, and failure modes of high-strength concrete-filled steel tubular (HSCFST) members under lateral impact, highlighting their superior impact resistance. Feng et al. (2022) conducted transverse continuous impact tests on cantilevered square CFST columns, examining the effects of impact mass and height. Their results demonstrated a positive correlation between cumulative plastic displacement and stiffness degradation with repeated impacts. Overall, previous research indicates that hollow tubular sections are prone to local deformations under impact loading. However, when these sections are filled with concrete, local deformations are significantly restricted, enhancing their ability to withstand greater lateral impact forces. Uslu et al. (2024) investigated 70 circular columns, which included both concrete-filled and hollow steel tubes, under axial loading. The study varied key parameters, such as concrete compressive strength (f_c), diameter-to-thickness (D/t), and length-to-diameter (L/D) ratios. Results showed that the ultimate axial load increased with higher f_c and D/t, but decreased with higher L/D. The findings were consistent with Eurocode 4, and finite element modeling slightly overestimated the axial capacity by about 5%.

Another effective solution to mitigate local buckling in hollow steel columns is the use of internal continuous stiffeners. These stiffeners reduce the likelihood of buckling in the outer shell by dividing the column into multiple smaller sections, known as cells, forming what is referred to as a multi-cell column (MCC).

Although research on MCCs as structural elements remains limited, their widespread use as energy absorbers in mechanical engineering has highlighted their potential advantages. This has drawn attention to their possible application as an alternative to concrete-filled tubular (CFT) columns, particularly in structures subjected to dynamic loads, where enhanced energy absorption is a highly desirable characteristic.

Numerous researchers have investigated the behavior of multi-cell columns (MCCs). Zhang et al. (2006) conducted analytical and numerical studies on the axial crushing of square MCCs, revealing that dividing a single-cell column into a 3×3 cell configuration increased its energy absorption by 50%. Similarly, Krolak et al. (2007, 2009) demonstrated that internally partitioning a column into multiple cells enhanced its load-carrying capacity and improved its buckling behavior. Bi et al. (2010) performed nonlinear finite element crash simulations on aluminum foam-filled single- and triple-cell hexagonal columns, showing that triple-cell composite columns exhibited greater crushing forces due to the corner effect. Song et al. (2012) conducted finite element analysis on axially loaded tubes with square, hexagonal, and octagonal cross-sections featuring origami-inspired patterns. The results revealed that these patterned tubes exhibited reduced initial peak forces and demonstrated more consistent and stable crushing behavior compared to traditional tubular designs. Yin et al. (2014) explored the energy absorption characteristics of foam-filled multi-cell thin-walled structures (FMTSs) through LS-DYNA simulations, while Sofi (2015), Wu et al. (2016), and Ahmed et al. (2017) examined the application of multi-cell thin-walled tubes in crashworthiness structures. Their findings consistently indicated that multi-cell thin-walled structures outperform single-cell structures in energy absorption. The energy absorption performance of MCCs is largely influenced by their shape and geometry. Yin et al. (2015) found that FMTSs with nine cells exhibited the best crashworthiness characteristics, while Ahmed et al. (2017) demonstrated that curvy stiffeners significantly improved energy absorption by increasing the mean crushing force and crush force efficiency compared to conventional configurations. Hassam et al. (2020) conducted experimental and finite element (FE) simulations on four multi-cell cross-shaped CFST stub columns, comparing their performance with existing CFST design formulas. Their results showed that these formulas underestimated the axial compressive capacity of cross-shaped CFST columns. Further investigations by Hassam et al. (2022) on ten multi-cell cross-shaped CFST columns examined key parameters such as slenderness ratio, width-to-thickness ratio of the steel tube, and load eccentricity. They found that the multi-cell configuration significantly improved concrete confinement. Yang et al. (2021) experimented with rectangular steel tubes and U-shaped steel plates to create three-cell cross-shaped steel tubes, testing nine slender columns under axial compression. Their findings indicated that increasing limb length enhanced load-bearing capacity while reducing ductility. More recently, Zheng et al. (2024) tested six stub columns under axial compression, varying cross-section form and concrete strength. Their results provided insights into failure patterns, ultimate strength, load-strain behavior, compressive stiffness, and ductility. They concluded that using longitudinal stiffeners or multi-cell configurations improves the axial compressive strength, stiffness, and ductility of cross-shaped CFST columns, further reinforcing the superior mechanical performance of multi-cell designs.

Previous research in this field has primarily focused on the behavior of axially loaded MCCs. To the best of the authors' knowledge, no prior studies have examined the response of MCCs to lateral impact loading. However, Tran et al. (2014) and Tran et al. (2015) theoretically investigated the behavior of multi-cell square tubes under oblique and axial impact loading, respectively.

In this study, a finite element (FE) model was developed using ABAQUS, a well-established and highly accurate finite element software, to analyze the response of both single-cell columns (SCCs) and multi-cell columns (MCCs) under lateral impact loading. Additionally, laboratory experiments were conducted on all specimens. A comparison between the numerical model and experimental results was performed, focusing on key parameters such as mid-point displacement and deformed shape. Further comparative analyses were conducted across all specimens, considering factors such as the rectangularity ratio of the cross-section (R), internal partitioning of the column into multiple cells, and concrete filling. The results, including mid-point displacement, impact force, energy absorption, and failure modes, were observed and discussed in detail.

2. Experimental Models and Test Setup

2.1. Specification of the tested specimens

Twelve specimens were prepared for testing, categorized into three groups. Each group consisted of two single-cell column (SCC) specimens—one filled with concrete (F) and the other empty (E)—and two multi-cell column (MCC) specimens, also with one filled (F) and one empty (E). Each group maintained a fixed height-to-width ratio (R=h/b), while all specimens shared the same cross-sectional area.

The total column length was 2860 mm, with an effective length of 2500 mm. Table 1 provides a detailed overview of the model dimensions, R ratios for each group, and the concrete filling conditions of the sections.

Table 1. Description of the tested specimens.

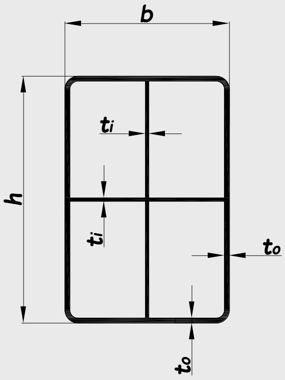

R	Condition	Dimensions (mm)				Concrete filling
		b	h	t_o	t_i	
1.00	SCC	100	100	5	–	E
						F
	MCC	100	100	4	2	E
						F
1.50	SCC	100	150	4	–	E
						F
	MCC	100	150	3	2	E
						F
2.25	SCC	100	225	3	–	E
						F
	MCC	100	225	2	2	E
						F

SCC: Single-cell column; MCC: Multi-cell column; E: Empty; F: Concrete-filled

2.2. Drop weight (impactor)

The drop weight was constructed from solid steel cylinders of varying diameters, welded together to form a unified mass. To ensure that the impact load was applied as a point load, the lower end of the drop weight was shaped into a conical section, as illustrated in Fig. 1. The total weight of the projectile was 57.85 kg.

2.3. Materials used for specimen fabrication

2.3.1. Concrete

A self-compacting concrete mix was used for specimen fabrication to facilitate placement and ensure complete filling of narrow sections, preventing voids and segregation.

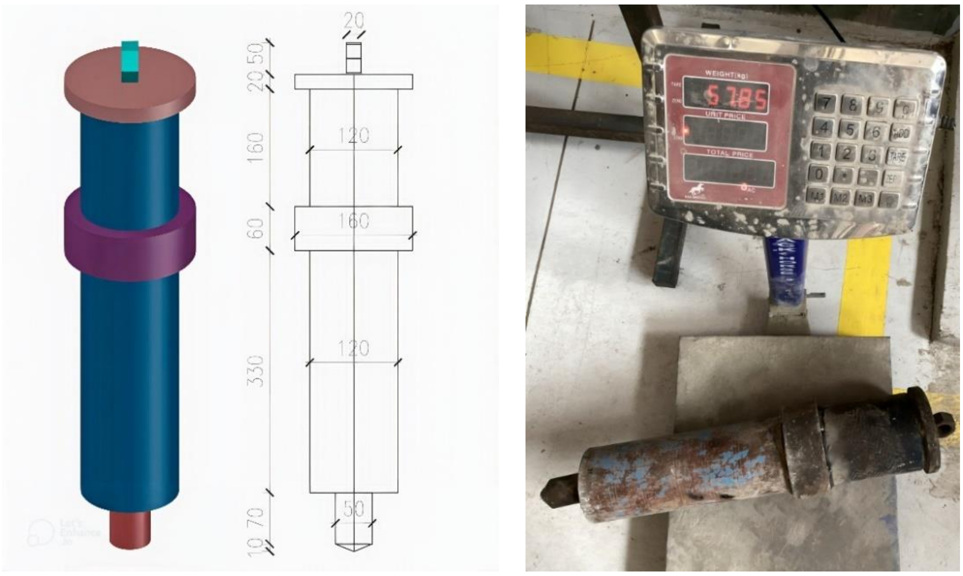

Fig. 1. Details of drop weight (impactor) (all dimensions are in mm).

Both the compressive and tensile strengths of the concrete mix were determined experimentally in accordance with the Egyptian Standard Specifications (ES1658-4/2008 and ISO1920-3:2004). The results showed a compressive strength of 46.3 MPa and a tensile strength of 4.08 MPa.

2.3.2. Material of steel tube and longitudinal stiffeners

The test specimens were fabricated using ST37 grade mild steel, with measured tensile strength (F_u) of 360 MPa and nominal yield strength (F_y) of 240 MPa.

2.4. Test setup and instrumentation

The tests in this study were conducted in the laboratory of the Institute of Concrete Structures Research at the Housing and Building National Research Center (HBRC). A custom-designed steel setup was used to support the tested specimens and provide the required end conditions. To ensure precise impact application, a PVC pipe with a diameter of 200 mm and a height of 3.00 meters was installed vertically at the center of each specimen. The pipe was secured using formwork to maintain vertical alignment and ensure that the load was applied precisely at the center of the sample. For a simply supported end condition, the columns were fully constrained in all displacement directions, effectively preventing any movement. In particular, displacement in the direction of the applied load was restricted. This restraint system included a U-shaped steel plate fixed to the support with bolts, as well as a steel rod to firmly secure the specimen, as illustrated in Fig. 2. The Linear Variable Differential Transformer (LVDT) device, shown in Fig. 3, was used to measure displacement over time, providing precise readings of the structure's deflection under both static and dynamic loads. Next, the specimen was positioned within the test setup, ensuring an effective span of 2500 mm. The LVDT device was placed directly beneath the center of the specimen to accurately record displacement data over time. Subsequently, a 57.85 kg impactor was released from a height of 3.3 meters through the PVC pipe, striking the specimen precisely at its center. The complete test setup is illustrated in Fig. 4.

3. Finite Element Modeling

To gain a deeper understanding of the behavior of multi-cell steel columns under impact loading, a finite element model was developed. In this study, ABAQUS/Explicit was used for analysis. ABAQUS/Explicit is a specialized analysis tool that employs an explicit dynamic finite element formulation. It is particularly well-suited for modeling short-duration, transient dynamic events such as impact and blast loads. Additionally, it efficiently handles highly nonlinear problems involving evolving contact conditions, such as forming simulations. The finite element models in this study were developed using the explicit nonlinear finite element code ABAQUS/Explicit. The following sections provide a detailed description of the FE model utilized in this research.

Fig. 2. Impact test support conditions.

Fig. 3. Displacement with time measurement device: (a) LVDT device; (b) Data logger and computer.

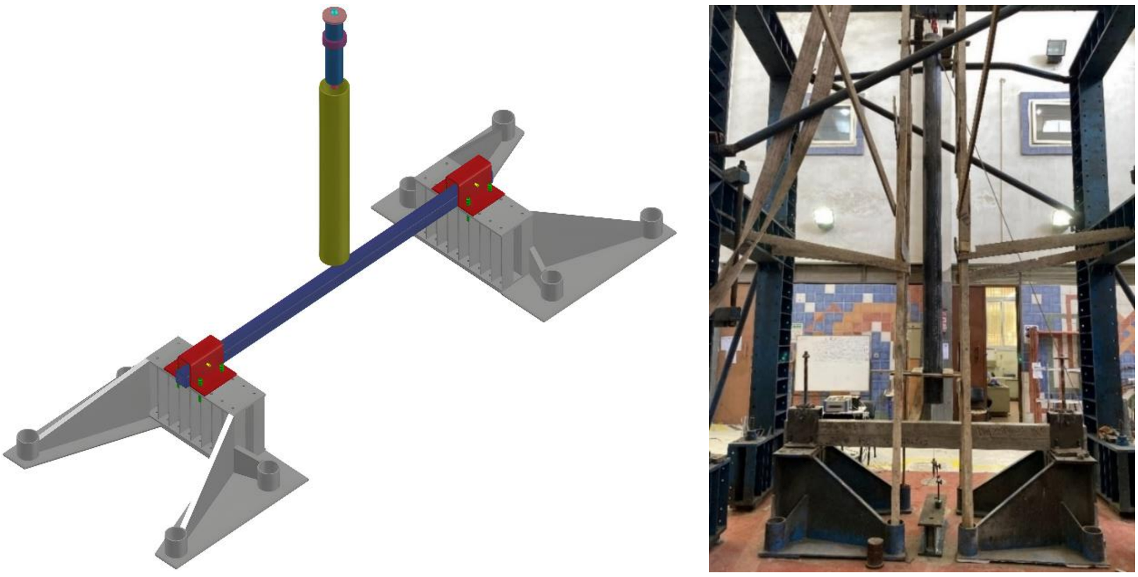

Fig. 4. Impact test setup.

3.1. Geometrical modeling

The steel tube and concrete were modeled using C3D8R elements, which are eight-node, reduced-integration solid elements. Each node of this element has three translational degrees of freedom, making it well-suited for defining contact surfaces necessary for applying impact loads. Additionally, it effectively integrates constitutive laws and is highly suitable for nonlinear dynamic analysis, allowing for finite strain and large-displacement rotations. A total of 7,752 elements were used to model the steel tube, while the concrete was represented by 24,168 elements. Meanwhile, the impactor was modeled as a rigid body using R3D4 elements and was discretized into 373 fine elements, as illustrated in Fig. 5.

Fig. 5. Mesh configuration of concrete-filled column under impact.

3.2. Material modeling

3.2.1. Material modeling of steel tube and longitudinal stiffeners

The modeling of the steel material requires defining the density, which was taken as 7,850 kg/m^3, the linear part in the stress-strain curve of steel and nonlinear part of the curve. The elastic properties are completely defined by giving the Young's modulus (E), and the Poisson's ratio (ν), the values of 210,000 MPa and 0.3 respectively.

The nonlinear part of the stress-strain curve of steel material was modeled using the PLASTIC option available in ABAQUS. It is used to describe the perfect plasticity or isotropic hardening behavior. Isotropic hardening means that the yield surface changes size uniformly in all directions such that the yield stress increases (or decreases) in all stress directions as plastic straining occurs. ABAQUS provides an isotropic hardening model, which is useful for cases involving gross plastic straining or in cases where the straining at each point is essentially in the same direction in strain space throughout the analysis. Although the model is referred to as a “hardening” model, strain softening or hardening followed by softening can be defined. If isotropic hardening is defined, the yield stress can be given as a tabular function of plastic strain and the yield stress at a given state is simply interpolated from the table of data. Since the buckling analysis involves large in-elastic strains, the nominal (engineering) static stress–strain curves were converted to true stress and logarithmic plastic true strain curves. The true stress (σ_{true}) and plastic true strain ($\varepsilon_{\mathrm{true}}^{\mathrm{pl}}$) were calculated using Eqs. (1) and (2) as given by ABAQUS. Figs. 6 and 7 show the relationship between the engineering and true stress strain curves.

$$\sigma_{true} = \sigma_{nom}\,(1 + \varepsilon_{nom}) \tag{1}$$

$$\varepsilon_{true}^{pl} = ln(1 + \varepsilon_{nom}) - \frac{\sigma_{true}}{E} \tag{2}$$

where E is the initial Young’s modulus; σ_{true} is the true stress; σ_{nom} is the nominal stress; $\varepsilon_{\mathrm{true}}$ is the true strain; and $\varepsilon_{\mathrm{nom}}$ is the nominal strain.

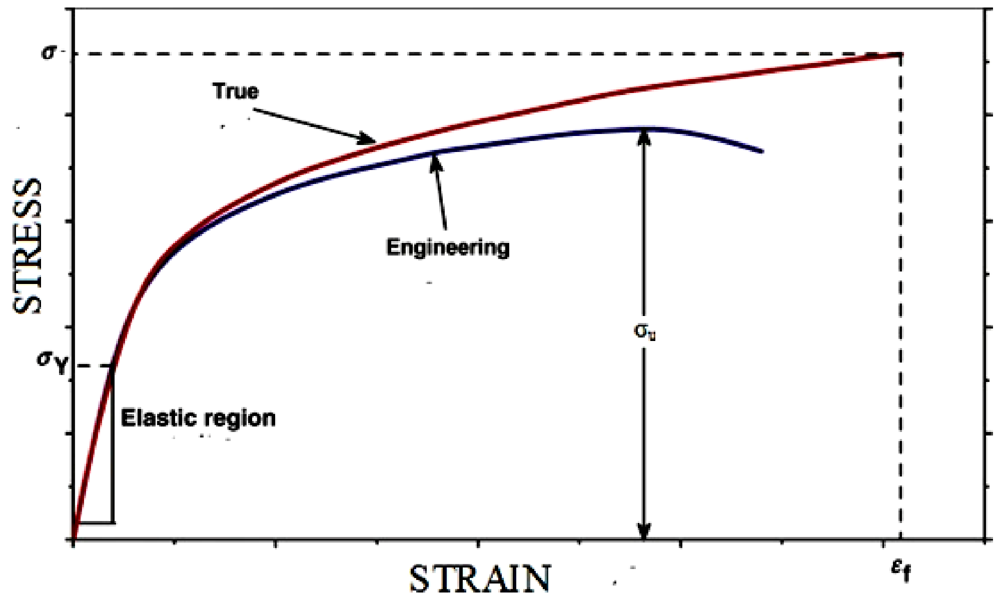

Fig. 6. The relationship between engineering and true stress-strain curves for steel (Elkady 2023).

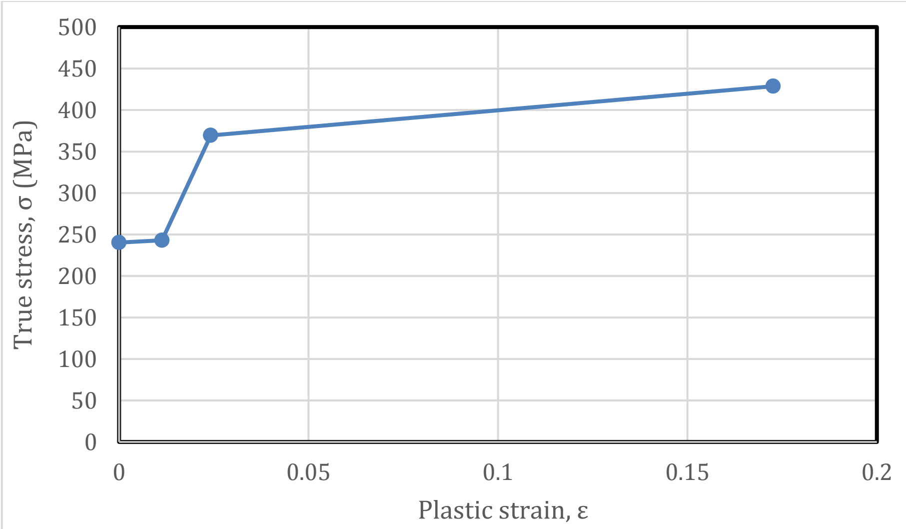

Fig. 7. True stress-plastic strain curve for ST37.

3.2.2. Material modeling of the confined concrete

Defining confined normal concrete requires specifying its density and stress-strain curve properties, which can be divided into two parts: elastic and plastic. The concrete material's mass density was defined using the DENSITY option in ABAQUS. The linear portion of the stress-strain curve was established using the ELASTIC option, where Young's modulus and Poisson's ratio (taken as 0.2) were specified to define the material's elastic behavior. The plastic behavior of concrete was modeled using the DRUCKER-PRAGER model in ABAQUS, which is widely used for simulating concrete and other quasi-brittle materials under various loading conditions, including cyclic loads. This model assumes that the primary failure mechanisms are tensile cracking and compressive crushing. The DRUCKER-PRAGER option was utilized to define a linear Drucker-Prager model with associated flow and isotropic hardening. The material parameters were set as follows: friction angle (β) = 20°, dilation angle (φ) = 35°, and the ratio of flow stress in triaxial tension to that in compression (K) = 0.8. The DRUCKER-PRAGER HARDENING option was used to define the equivalent uniaxial stress-strain curves for confined concrete. The confinement effect in concrete-filled box steel columns depends on the D/t ratio, where D is depth. Columns with a high D/t ratio provide weak confinement, leading to premature failure due to local buckling of the steel tubes. Conversely, columns with a low D/t ratio offer strong confinement due to increased thickness, enhancing the strength of the infill concrete and allowing it to be treated as confined concrete. The relationship between the equivalent uniaxial stress-strain curves for both unconfined and confined concrete is illustrated in Fig. 8, as presented by Ellobody et al. (2006), where f_c represents the unconfined concrete cylinder compressive strength, equal to $0.8 \times F_{cu}$, and F_{cu} is the unconfined concrete cube compressive strength. The corresponding unconfined strain (ε_c) is taken as 0.003, as recommended by ACI specifications. Mander et al. (1988) proposed Eqs. (3) and (4) to describe stress-strain relationships, from which the confined concrete compressive strength (f_{cc}) and the corresponding confined strain (ε_{cc}) can be determined.

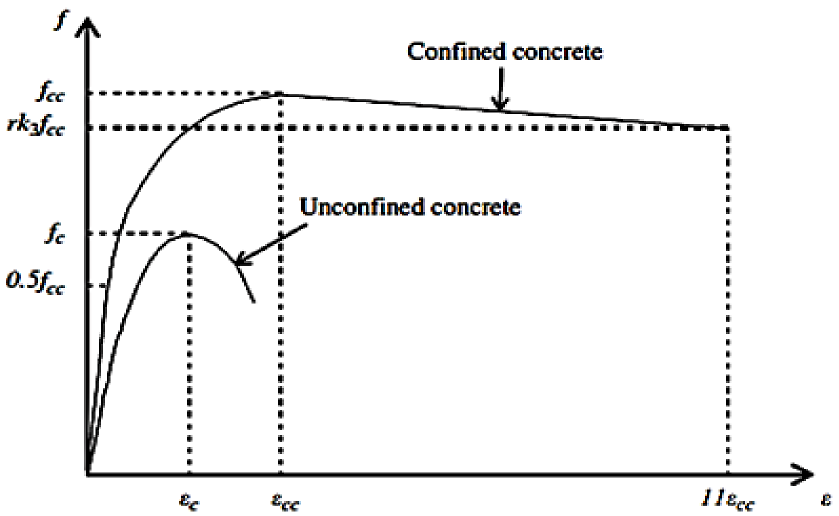

Fig. 8. Equivalent uniaxial stress-strain curve for confined and unconfined concrete (Ellobody et al. 2006).

$$f_{cc} = f_c + k_1 f_1 \quad (3)$$

$$\varepsilon_{cc} = \varepsilon_c(1 + k_2 \frac{f_1}{f_c}) \quad (4)$$

where f_1 is the confining pressure from steel tube that depends on the D/t ratio and the steel box yield stress; and k_1 and k_2 are coefficients that depend on lateral pressure and concrete mix.

Based on their tests, Richart et al. (1928) found the average values of those coefficients are k_1=4.1 and k_2=5k_1. Also, tests of Balmer (1949) showed that k_1 has an average value of 5.6, and increases by decreasing lateral pressures.

The approximate value of (f_1) can be obtained from empirical Eqs. (5) or (6) given by Hu et al. (2003), where f_{yd} is the yield strength of the steel tube.

$$f_1/f_{yd} = 0.043646 - 0.000832(D/t)$$

$$21.7 \leq (D/t) \leq 47 \quad (5)$$

$$f_1/f_{yd} = 0.006241 - 0.0000357(D/t)$$

$$47 \leq (D/t) \leq 150 \quad (6)$$

The stress strain relation diagram of concrete is also divided into three parts. The first part is the initially assumed elastic range to the proportional limit stress. The value of the proportional limit stress is taken as 0.5(f_{cc}) as given by Hu et al. (2003). The initial Young's modulus of confined concrete (E_{cc}) is reasonably calculated using the empirical Eq. (7) given by ACI 318-19 (2019).

$$E_{cc} = 4700\sqrt{f_{cc}} \quad \text{(MPa)} \quad (7)$$

The second part of the equivalent uniaxial stress–strain curve for confined concrete was determined by Eq. (8), which is a common equation proposed by Saenz (1964). This part starts from the proportional limit stress 0.5(f_{cc}) to the confined concrete strength (f_{cc}). This equation is used to represent the multidimensional stress and strain values for the equivalent uniaxial stress and strain values. The unknowns of the equation are the uniaxial stress (f) and strain (ε) values. Substituting the strain values (ε) between the proportional strain, which is equal to ($0.5f_{cc}/E_{cc}$), and the confined strain (ε_{cc}) gives the corresponding value of the confined concrete strength.

$$f = \frac{E_{cc}\varepsilon}{1+(R+R_E-2)(\varepsilon/\varepsilon_{cc}) - (2R-1)(\varepsilon/\varepsilon_{cc})^2 + R(\varepsilon/\varepsilon_{cc})^3} \quad (8)$$

where R_E and R values are calculated from Eqs. (9) and (10), respectively.

$$R_E = \frac{E_{cc}\varepsilon_{cc}}{f_{cc}} \quad (9)$$

$$R = \frac{R_E(R_\sigma - 1)}{(R_\varepsilon - 1)^2} - \frac{1}{R_\varepsilon} \quad (10)$$

where R_σ and R_ε are constants, values taken to be equal to 4.0, as recommended by Hu and Schnobrich (1989).

The third part of the confined concrete stress–strain curve is the descending part from the confined concrete strength (f_{cc}) to a value lower than or equal to $r \cdot k_3 \cdot f_{cc}$ with the corresponding strain of 11ε_{cc}. The reduction factor (k_3) depends on the D/t ratio and the steel tube yield stress (f_y). The approximate value of k_3 can be calculated from empirical Eqs. (11) and (12) given by Hu et al. (2003).

$$k_3 = 1 \qquad 21.7 \leq (D/t) \leq 47 \quad (11)$$

$$k_3 = 0.0000339\left(\frac{D}{t}\right)^2 - 0.0100085\left(\frac{D}{t}\right) + 1.3491$$

$$47 \leq \left(\frac{D}{t}\right) \leq 150 \quad (12)$$

The reduction factor (r) was introduced by Ellobody et al. (2006), based on the experimental investigation conducted by Giakoumelis and Lam (2004). The value of r is taken as 1.0 for concrete with cube strength (f_{cu}) equal to 30 MPa. The value of r is taken as 0.5 for concrete with f_{cu} greater than or equal to 100 MPa.

3.3. Contact and interaction

The interface element was utilized to model the contact between the concrete and the steel tube. This element consists of master and slave surfaces that correspond to the matching contact faces of the steel tube and concrete elements. According to Capilla and García (2013), the friction coefficient for simulating the interaction between concrete and steel tubes in composite columns ranges from 0.2 to 0.8. In this study, a friction coefficient of 0.8 was adopted. The interface element permits surface separation under tensile forces but prevents penetration between the contacting surfaces. Additionally, the interaction between the column and the projectile was modelled as hard contact to accurately represent the impact conditions.

3.4. Boundary conditions

To simulate the motion of the impactor, it was given an initial velocity (8.05 m/s) in a direction perpendicular to the column while the rest of DOFs were constrained. The column was given a hinged-hinged boundary condition to simulate test.

4. Comparison of Results

In the following sections, the results obtained from analysis are compared with the experimental results. The compared results include shape of failure and Maximum displacement due to impact loading.

4.1. Deformed shape of column after impact

Figs. 9–20 represent a comparison between the deformed shape of the 12-tested specimens and the corresponding FE models.

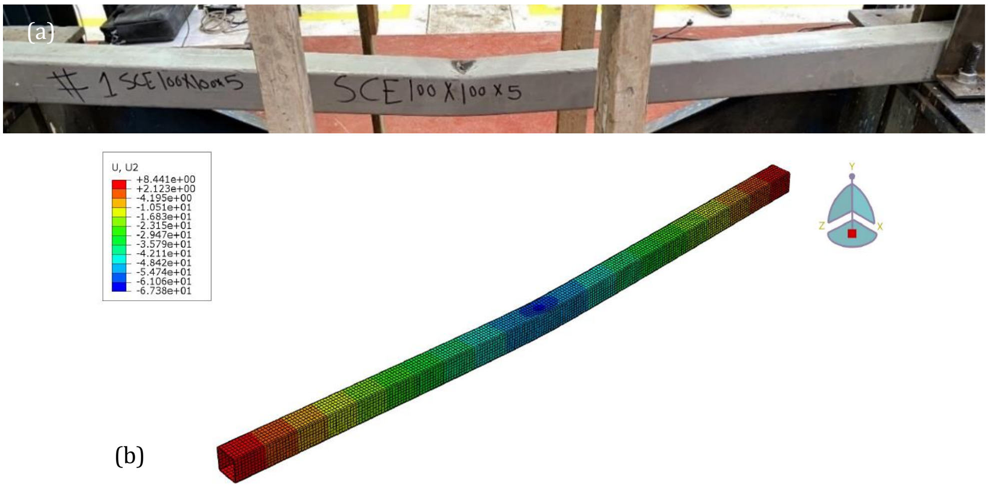

Fig. 9. Deformed shape of 100X100X5 empty single-cell column (SCC-E):
(a) Deformed shape of tested specimen; (b) Deformed shape of tested specimen's FE model.

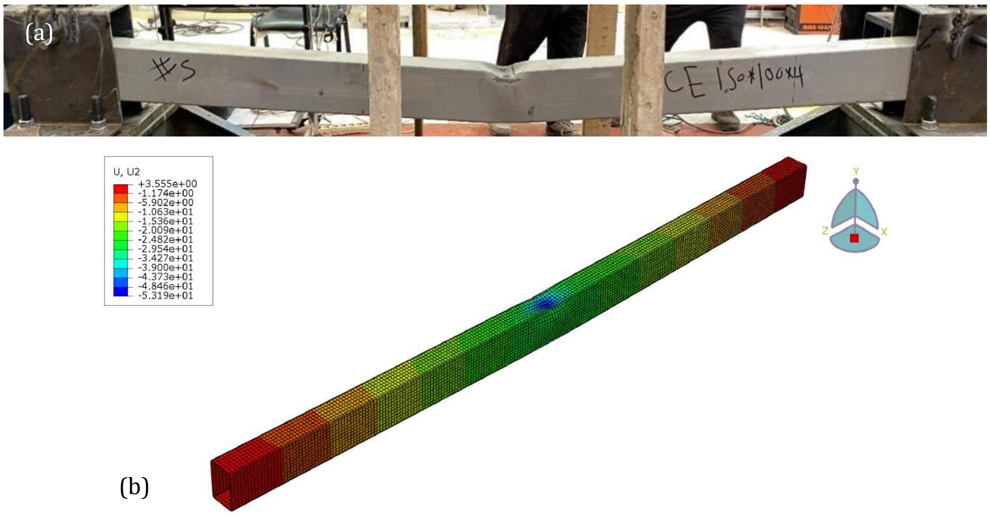

Fig. 10. Deformed shape of 100X150X4 empty single-cell column (SCC-E):
(a) Deformed shape of tested specimen; (b) Deformed shape of tested specimen's FE model.

Fig. 11. Deformed shape of 100X225X3 empty single-cell column (SCC-E):
(a) Deformed shape of tested specimen; (b) Deformed shape of tested specimen's FE model.

Fig. 12. Deformed shape of 100X100X5 filled single-cell column (SCC-F):
(a) Deformed shape of tested specimen; (b) Deformed shape of tested specimen's FE model.

Fig. 13. Deformed shape of 100X150X4 filled single-cell column (SCC-F):
(a) Deformed shape of tested specimen; (b) Deformed shape of tested specimen's FE model.

Fig. 14. Deformed shape of 100X225X3 filled single-cell column (SCC-F):
(a) Deformed shape of tested specimen; (b) Deformed shape of tested specimen's FE model.

Fig. 15. Deformed shape of 100X100X4X2 empty multi-cell column (MCC-E):
(a) Deformed shape of tested specimen; (b) Deformed shape of tested specimen's FE model.

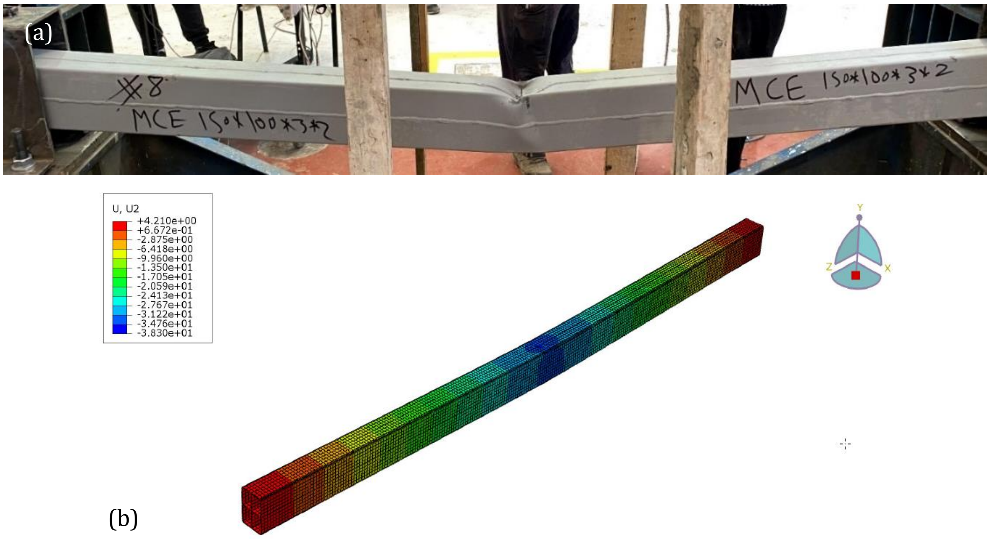

Fig. 16. Deformed shape of 100X150X3X2 empty multi-cell column (MCC-E):
(a) Deformed shape of tested specimen; (b) Deformed shape of tested specimen's FE model.

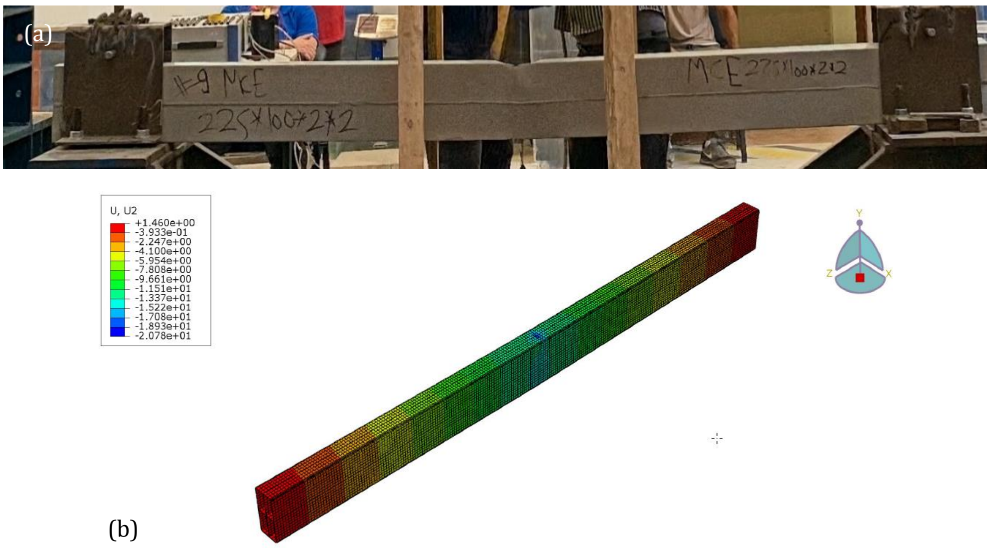

Fig. 17. Deformed shape of 100X225X2X2 empty multi-cell column (MCC-E):
(a) Deformed shape of tested specimen; (b) Deformed shape of tested specimen's FE model.

Fig. 18. Deformed shape of 100X100X4X2 filled multi-cell column (MCC-F):
(a) Deformed shape of tested specimen; (b) Deformed shape of tested specimen's FE model.

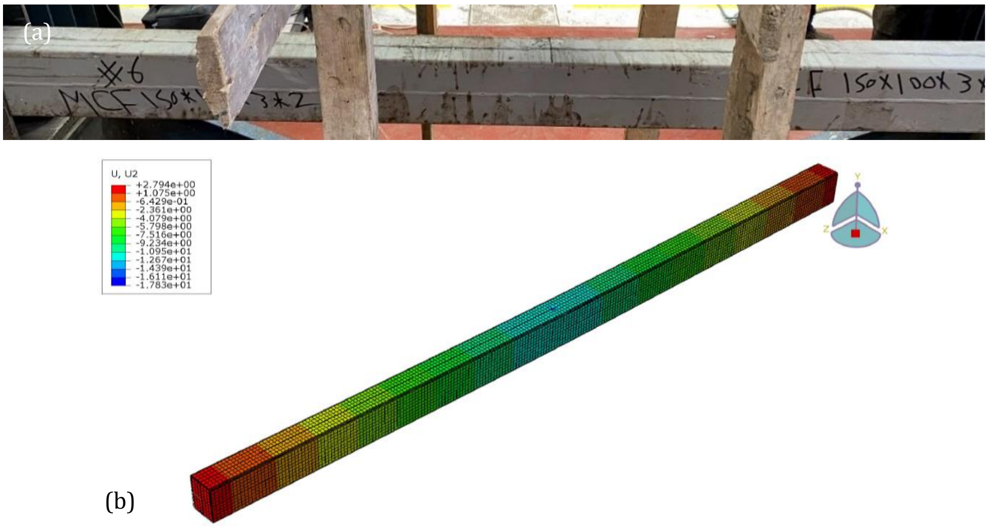

Fig. 19. Deformed shape of 100X150X3X2 filled multi-cell column (MCC-F):
(a) Deformed shape of tested specimen; (b) Deformed shape of tested specimen's FE model.

Fig. 20. Deformed shape of 100X225X2X2 filled multi-cell column (MCC-F):
(a) Deformed shape of tested specimen; (b) Deformed shape of tested specimen's FE model.

4.2. Max displacement at mid-point of sample

Table 2 provides a comparison between maximum displacements in experimental and analytical models. It is clear that the FE models represents the tests on steel and composite tubular columns under impact loading accurately.

5. Results of Analytical Models

Numerical analyses of the 12 models were performed under the same conditions. The main outcomes from analysis include maximum displacement at mid-span, maximum impact force, mode of failure and energy absorption.

Table 2. Comparison between experimental and FE models.

Concrete filling	*R*	Sample label	Maximum deflection (mm)		Difference (%)
			Experimental	FE model	
Empty columns	1.00	SCC-E (100X100X5)	46.485	52.500	11.46
		MCC-E (100X100X4X2)	60.937	59.165	-2.99
	1.50	SCC-E (100X150X4)	26.369	24.707	-6.73
		MCC-E (100X150X3X2)	29.993	32.072	6.48
	2.25	SCC-E (100X225X3)	9.522	10.424	8.65
		MCC-E (100X225X2X2)	18.564	18.092	-2.61
Concrete-filled columns	1.00	SCC-F (100X100X5)	38.644	34.715	-11.32
		MCC-F (100X100X4X2)	35.464	37.864	6.34
	1.50	SCC-F (100X150X4)	8.976	9.501	5.52
		MCC-F (100X150X3X2)	12.588	12.537	-0.40
	2.25	SCC-F (100X225X3)	4.251	4.689	9.34
		MCC-F (100X225X2X2)	5.736	5.221	-9.87

5.1. Mid-point displacement

The time-displacement curves for all models are illustrated in Figs. 21 and 22. The displacement of the lower side midpoint of each model was chosen as a reference point, as it provides a clear indication of model rigidity and strength. Fig. 21 compares the displacement of all concrete-filled single and multi-cell column models. It is evident that single-cell models exhibit smaller displacements compared to multi-cell columns with the same cross-sectional area. Specifically, the maximum displacement of the (100×100) single-cell model is reduced by approximately 8.32% compared to its multi-cell counterpart. Similarly, reductions of about 24.22% and 10.19% are observed for the (150×100) and (225×100) models, respectively. Fig. 22 presents a comparison of all empty single and multi-cell column models, showing that single-cell models consistently experience smaller displacements than multi-cell columns of the same cross-sectional area. The maximum displacement of the (100×100) single-cell empty model is reduced by approximately 11.26% compared to the multi-cell empty model. Additionally, reductions of about 22.96% and 42.38% are observed for the (150×100) and (225×100) models, respectively. A summary of the maximum displacement values for all models is provided in Fig. 23.

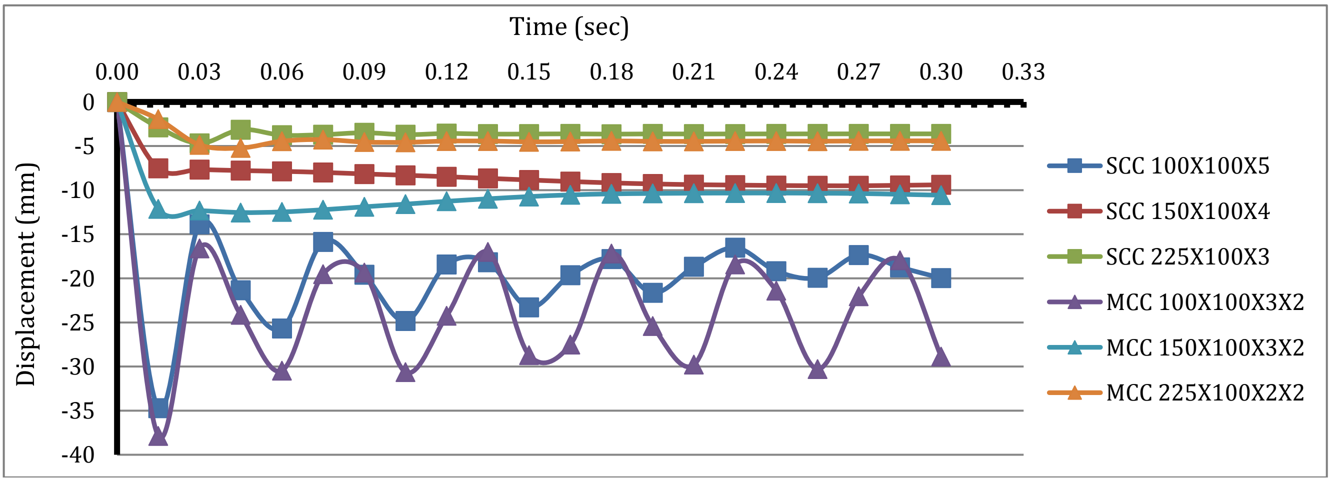

Fig. 21. Time-displacement relationships for concrete-filled columns.

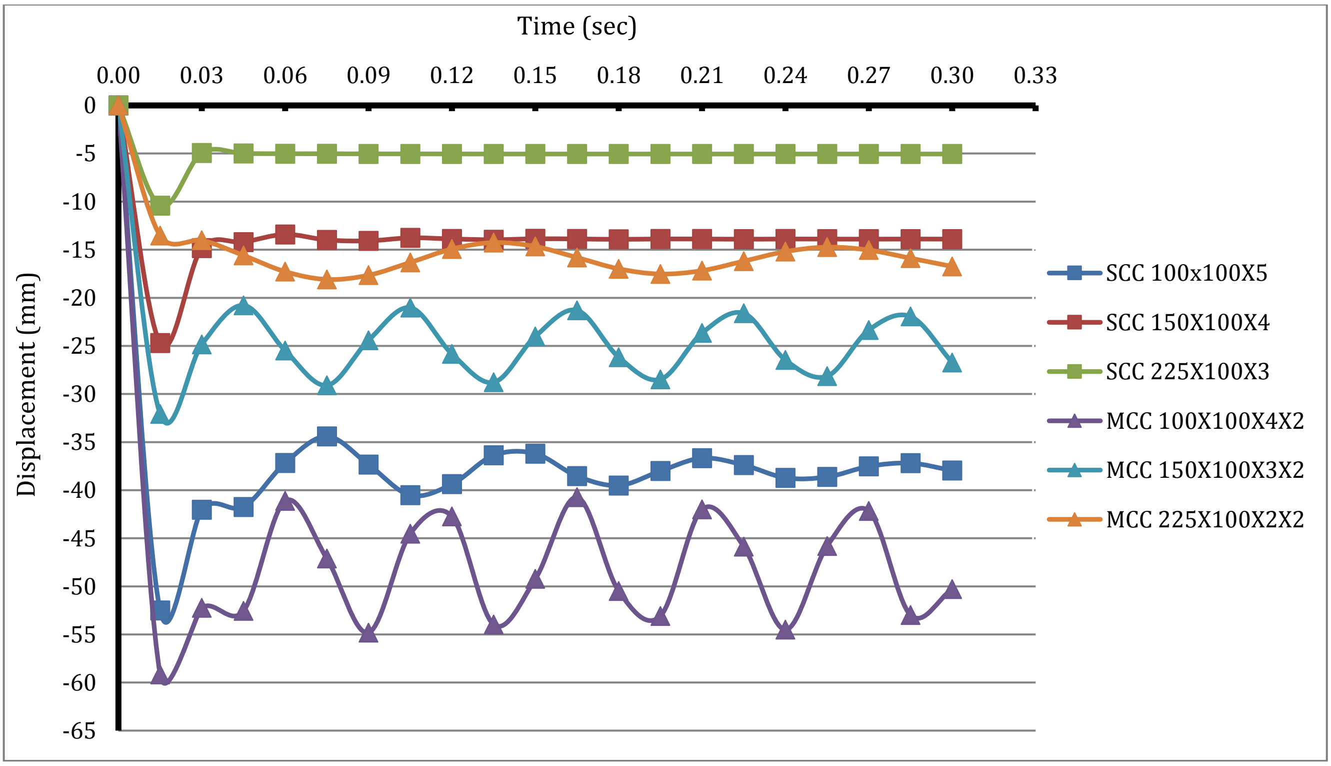

Fig. 22. Time-displacement relationships for empty columns.

These results are logical, as global deformation is primarily influenced by the moment of inertia. When two columns have the same cross-sectional area, the single-cell column possesses a greater moment of inertia than the multi-cell column. This is because, in single-cell columns, the material is concentrated along the periphery, placing it farther from the section's center of gravity, thereby enhancing rigidity and reducing deformation.

As illustrated in Fig. 23, the concrete-filled single-cell model with dimensions 225×100 mm exhibits the lowest maximum displacement of 4.689 mm, while the empty multi-cell model with dimensions 100×100 mm has the highest maximum displacement of 59.165 mm.

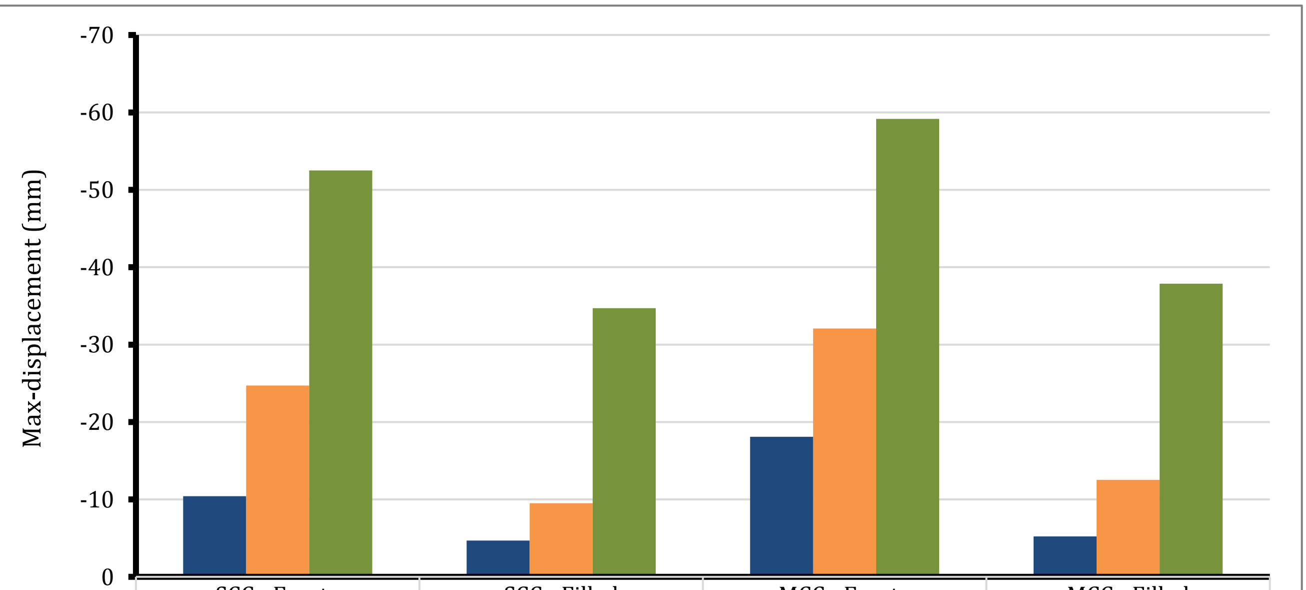

	SCC - Empty	SCC - Filled	MCC - Empty	MCC - Filled
225x100	-10.424	-4.689	-18.092	-5.221
150x100	-24.707	-9.501	-32.072	-12.537
100x100	-52.500	-34.715	-59.165	-37.864

Fig. 23. Maximum displacements for all models.

5.2. Impact load capacity

Fig. 24 summarizes and explains the maximum impact forces for all models. The determination of maximum impact force provides a more precise correlation with absorbed energy. The figure indicates that the concrete-filled single-cell model with dimensions 225×100 mm exhibits the highest impact force among all models. This highlights the superior impact resistance of concrete-filled models compared to empty ones, as well as the influence of model dimensions on the amount of impact force that can be sustained.

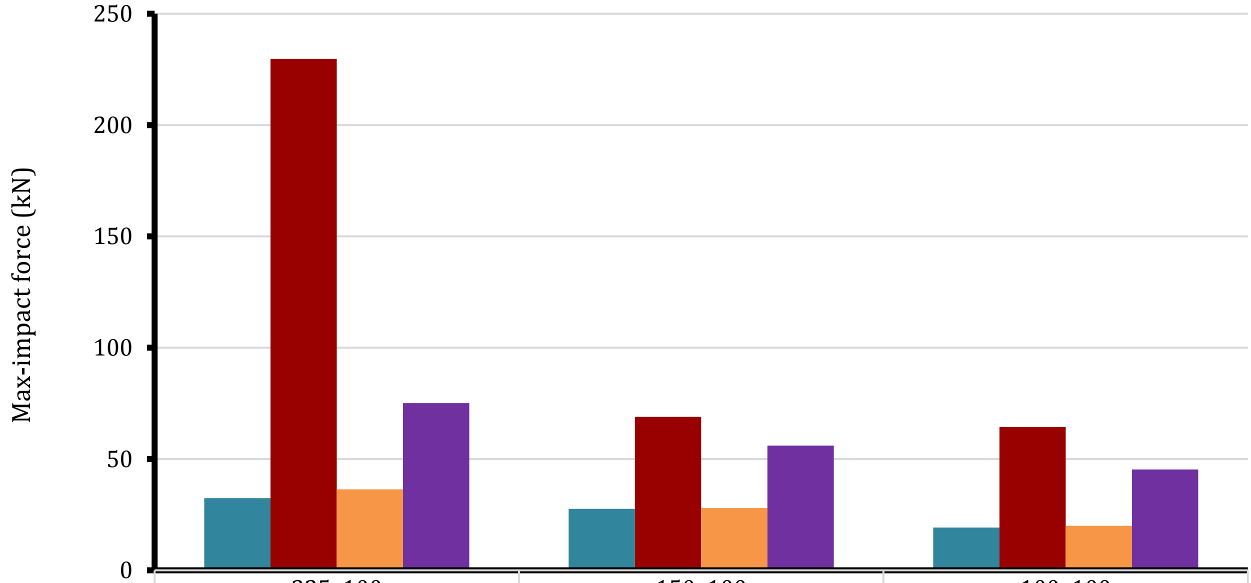

	225x100	150x100	100x100
SCC - Empty	32.425	27.630	19.161
SCC - Filled	229.715	68.956	64.376
MCC - Empty	36.366	27.941	19.967
MCC - Filled	75.108	55.989	45.291

Fig. 24. Maximum impact force for all models.

5.3. Energy absorption

When a structure is impacted by a moving object, the kinetic energy of the projectile is transformed into strain energy within the structure, which is partially dissipated through local plastic deformation and strain energy. Energy-absorbing structures undergo significant deformation to absorb the impact energy while maintaining their structural integrity. Yin et al. (2014, 2015) introduced the concept of "crashworthiness indicators" to evaluate a structure's ability to absorb energy. These indicators include energy absorption (EA), specific energy absorption (SEA), mean crushing force (MCF), and crash load efficiency (CLE). Energy absorption (EA) can be defined in terms of the deflection of the structural element. According to ACI Committee 363, energy absorption is determined by the toughness of mid-span deflection (displacement). This is calculated as the total area under the load-deflection curve from the origin to the point of rupture, as expressed in Eq. (13).

$$EA = \int_0^d F(x)\, dx \tag{13}$$

where d is the crushing displacement and F denotes the impact force.

For all column models with dimensions 225×100 mm, the highest and lowest energy absorption values were recorded at 4214.972 J and 1204.036 J for the concrete-filled single-cell and empty single-cell models, respectively. The increased energy absorption in filled models can be attributed to the enhanced stiffness provided by the concrete filling, which helps distribute the impact force over a larger cross-sectional area. Across all model groups, the concrete-filled single-cell column exhibits the highest energy absorption, while the empty single-cell model has the lowest. In multi-cell models, the energy absorbed by the empty multi-cell column is either greater than or nearly equal to that of the concrete-filled multi-cell column. This performance may be due to the presence of cross-steel webs, which contribute to stiffness, reducing the impact of concrete filling on overall rigidity.

However, in models with dimensions 100×100 mm, the concrete-filled multi-cell model absorbs more energy than its empty counterpart. This is because, in these models, stiffness is nearly equal along both the horizontal and vertical axes, making the filled multi-cell model more rigid and better able to absorb impact energy. The energy absorption of all models is illustrated in Fig. 25.

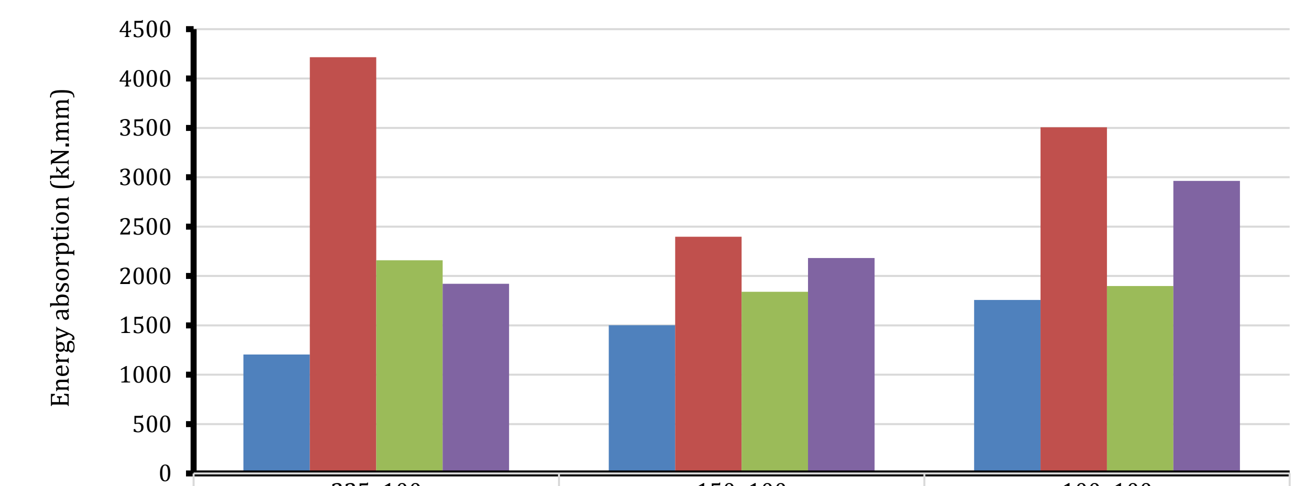

	225x100	150x100	100x100
SCC - Empty	1204.036	1501.363	1757.432
SCC - Filled	4214.972	2397.053	3506.259
MCC - Empty	2159.766	1839.125	1897.848
MCC - Filled	1920.320	2181.389	2962.698

Fig. 25. Energy absorption for all models.

5.4. Failure modes

For all empty single-cell column models, the primary failure mode was local buckling. In contrast, in all concrete-filled column models, the presence of concrete significantly reduced the effects of local buckling. A similar effect was observed in empty multi-cell column models, where the presence of cross-steel webs helped mitigate local buckling. Fig. 26 illustrates the local buckling failure of empty single-cell column models with various dimensions under impact loading. Figs. 27 and 28 depict the global deformation of both single and multi-cell models, including concrete-filled and empty multi-cell columns, under impact loading. These figures clearly highlight the differences in local buckling behavior between empty and concrete-filled column models.

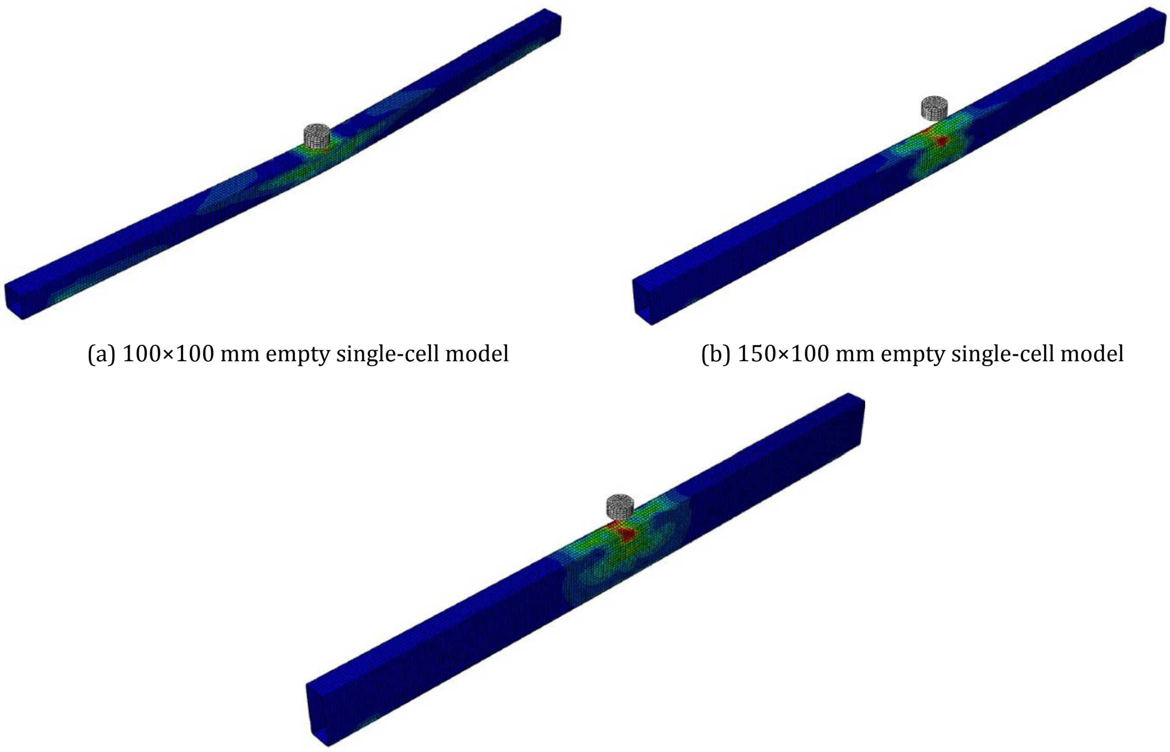

(a) 100×100 mm empty single-cell model

(b) 150×100 mm empty single-cell model

(c) 225×100 mm empty single-cell model

Fig. 26. Local buckling effects for empty single-cell models after impact load.

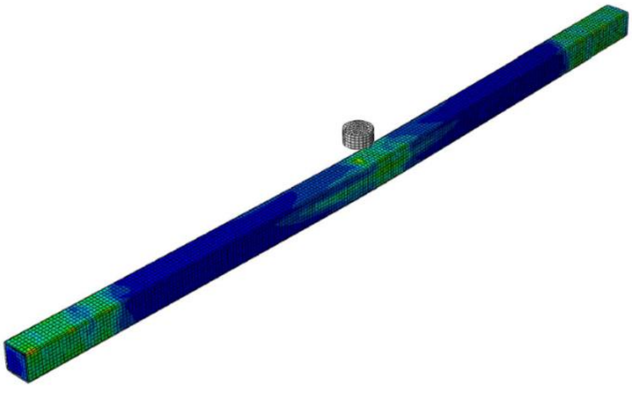

(a) 100×100 mm filled single-cell model

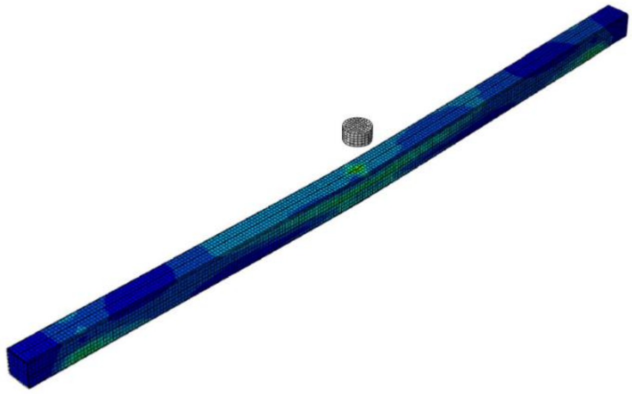

(b) 100×100 mm filled multi-cell model

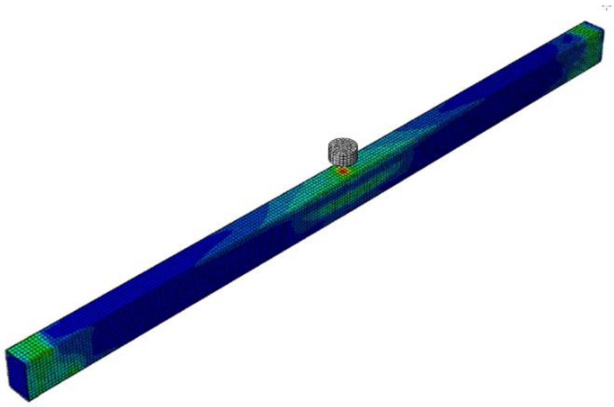

(c) 150×100 mm filled single-cell model

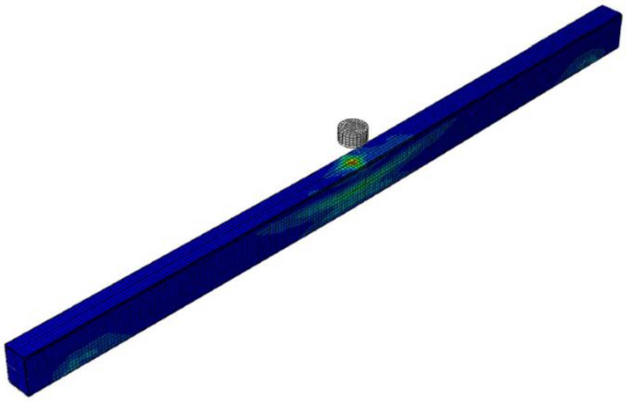

(d) 150×100 mm filled multi-cell model

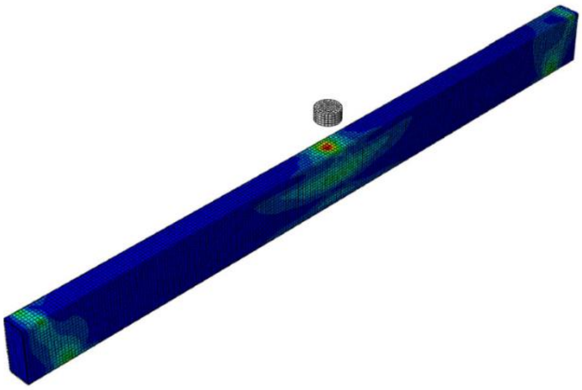

(e) 225×100 mm filled single-cell model

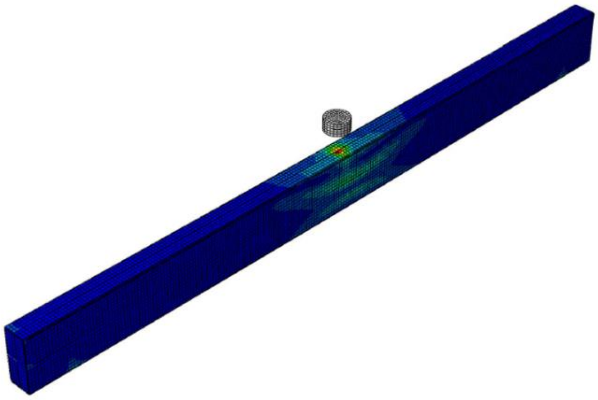

(f) 225×100 mm filled multi-cell model

Fig. 27. Global deformations for concrete-filled single- and multi-cell models after impact load.

5.5. Rectangularity ratio effect

The rectangularity ratio, R, is the ratio of the height to the width of the section, which is one of the most important factors that have been considered in the current study. The effects of rectangularity ratio on both force - displacement and absorbed energy are presented in Figs. 29–31.

Fig. 29 illustrates the effect of R on maximum impact force which can be noted that max-impact force increases with increasing R. The increasing percentage has reached 257% when the R ratio was increased by 2.25% in case of filled single-cell model. In all models, there is a marked increase in maximum impact force with increasing R. Fig. 30 illustrates effect of R on maximum mid-point displacement which decreases with increasing of R. For example, empty multi-cell model recorded maximum mid-point displacement of 59.165 mm when R equals to 1 and recorded 18.092 mm when R equals to 2.25 with decreasing percentage of 69.42%. In all models, there is a marked decrease in maximum mid-point displacement with increasing R. Fig. 31 illustrates effect of R on energy absorbed which shows a difference in the effect of R on the amount of energy absorbed which decreases when the ratio reaches 1.50 and then increase when the ratio reaches 2.25 in case of filled single-cell. But in case of empty single-cell, increasing R leads to deceasing in amount of energy absorbed by model which may be because dissipation of energy in local buckling under falling impactor.

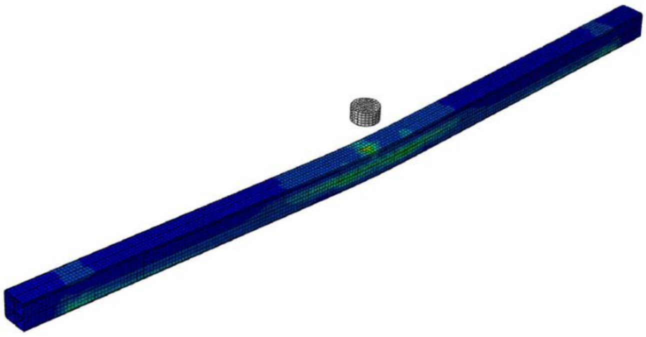

(a) 100×100 mm empty multi-cell model

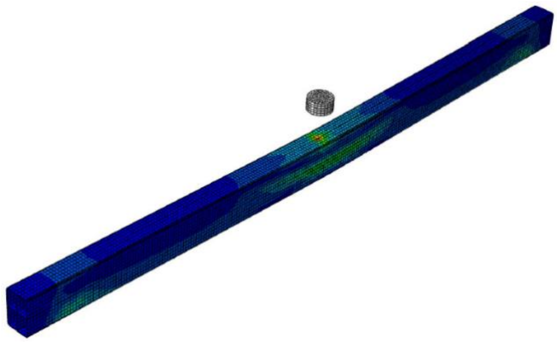

(b) 150×100 mm empty multi-cell model

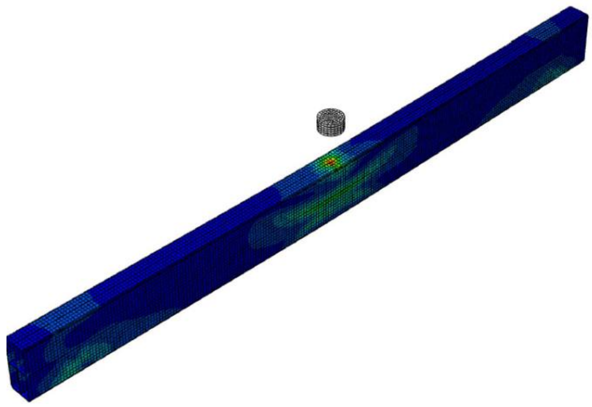

(c) 225×100 mm empty multi-cell model

Fig. 28. Global deformations for empty multi-cell models after impact load.

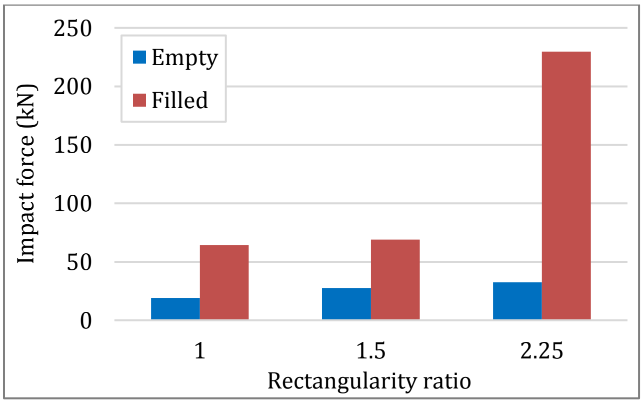

(a) Single-cell models

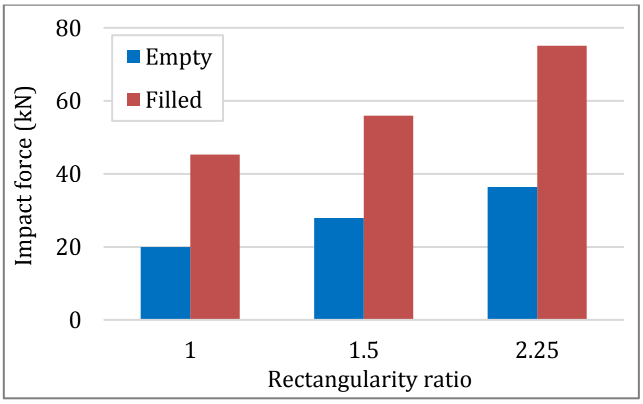

(b) Multi-cell models

Fig. 29. Effect of rectangularity ratio on maximum impact force.

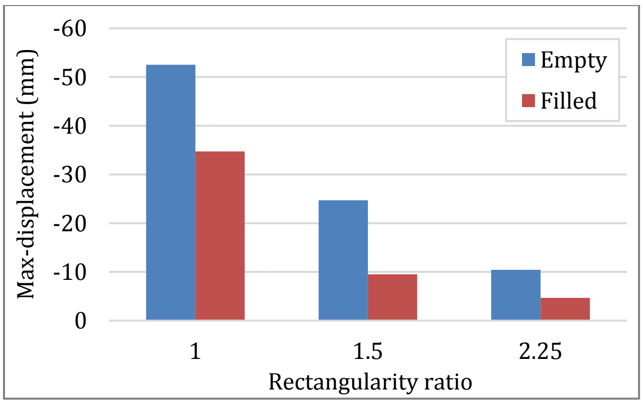

(a) Single-cell models

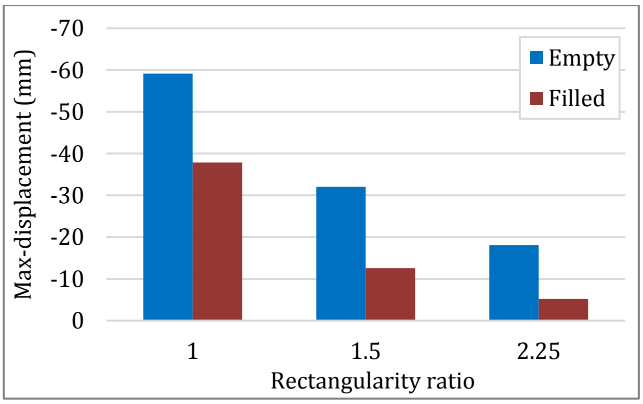

(b) Multi-cell models

Fig. 30. Effect of rectangularity ratio on maximum mid-point displacement.

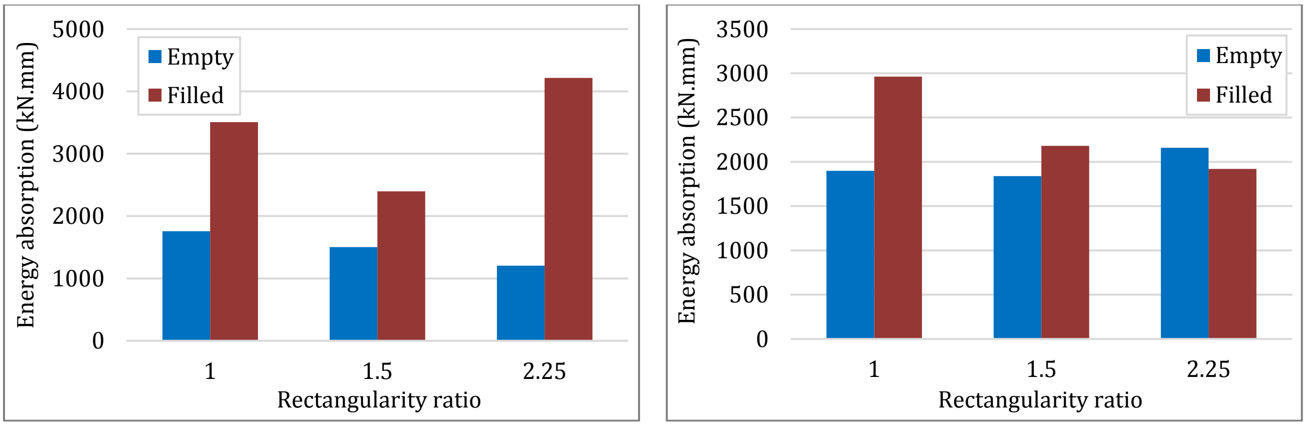

(a) Single-cell models (b) Multi-cell models

Fig. 31. Effect of rectangularity ratio on energy absorption.

6. Conclusions

This study examined the behavior of single and multi-cell steel columns, both with and without concrete filling, and analyzed the effect of section dimensions (rectangularity ratio) on their performance.

Based on the experimental and modeling results, the following conclusions were drawn:

- For all models, single-cell columns exhibited lower displacement values compared to multi-cell columns. This can be attributed to the influence of the moment of inertia on global deformations. Given the same cross-sectional area, a single-cell column has a greater moment of inertia than a multi-cell column, as its material is distributed along the periphery, placing it farther from the section's center of gravity.
- The internal division of a column into multiple cells significantly reduced local buckling under impact by increasing the section's local stiffness. A similar stiffening effect was observed with concrete filling.
- For empty models, multi-cell columns absorbed more energy than single-cell columns, indicating that the impactor's kinetic energy was effectively converted into strain energy within the column, which was dissipated through local plastic deformation. However, concrete-filled models did not follow this trend, as concrete, unlike steel, is a brittle material that lacks the ability to undergo large deformation to absorb impact energy without compromising its structural integrity.
- The rectangularity ratio (R) had a significant effect on impact force and mid-point displacement. An increase of 2.25% in R resulted in an increase of 257% in impact force and a reduction of 69.42% in mid-point displacement.
- For empty single-cell columns, an increase in R led to a decrease in energy absorption. This may be due to energy dissipation through local buckling under the falling impactor.

Acknowledgements

None declared.

Funding

The authors received no financial support for the research, authorship, and/or publication of this manuscript.

Conflict of Interest

The authors declared no potential conflicts of interest with respect to the research, authorship, and/or publication of this manuscript.

Author Contributions

All of the authors made substantial contributions to conception and design, or acquisition of data, or analysis and interpretation of data; were involved in drafting the manuscript or revising it critically for important intellectual content; and gave final approval of the version to be published.

Data Availability

The datasets created and/or analyzed during the current study are not publicly available, but are available from the corresponding author upon reasonable request.

References

ABAQUS User's Guide (2014). Abaqus Documentation User's Guide. s.l.: Dassault Systemes, Simulia Corp.

ACI 318-19 (2019). Building Code Requirements for Structural Concrete and Commentary. American Concrete Institute, Farmington Hills, MI.

Ahmed N, Xue P, Kamran M, Zafar N, Mustafa A, Zahran M (2017). Investigation of the energy absorption characteristics of metallic tubes with curvy stiffeners under dynamic axial crushing. *Latin American Journal of Solids and Structures*, 14(7), 1443-1463.

Al-Thairy H (2012). Behaviour and Design of Steel Columns Subjected to Vehicle Impact. *Ph.D. thesis*, University of Manchester, Manchester, UK.

Balmer GG (1949). Shearing strength of concrete under high triaxial stress computation of Mohr's envelope as a curve. SP-23, Structural Research Laboratory, U.S. Bureau of Reclamation.

Bambach M, Zhao H, Grzebieta R (2008). Hollow and concrete filled steel hollow sections under transverse impact loads. *Engineering Structures*, 30(10), 2859-2870.

Bedage SD, Shinde DN (2015). Concrete filled steel tubes subjected to axil compression. *International Journal of Research in Engineering and Technology*, 4(6), 459-464.

Bi J, Fang H, Wang Q, Ren X (2010). Modeling and optimization of foam-filled thin-walled columns for crashworthiness designs. *Finite Elements in Analysis and Design*, 46(9), 698–709

Campbell A (1994). Axial Load Capacity of Circular Steel Tube Columns Filled with High Strength Concrete. *M.Sc. thesis,* Victoria University of Technology, Victoria, Australia.

Capilla AE, García MLR (2013). Finite element modelling of innovative concrete-filled tubular columns under room and elevated temperatures. In: *European Project FRISCC "Fire Resistance of Innovative and Slender Concrete Filled Tubular Composite Columns"*, Engineering, Materials Science (Editor UPV).

Chu K (2014). Axial load behaviour of steel tube columns in-filled with various high-performance concretes. *M.Sc. Thesis,* Ryerson University, Toronto, Ontario, Canada.

EOS1658-4/2008 (2008) Testing of concrete – Part 3: Making and curing test specimens (ISO 1920-3:2004 equivalent). Egyptian Organization for Standardization and Quality, Cairo, Egypt.

Elkady A (2023). ABAQUS_SteelMat_Generator: A tool for generating metal plastic and damage parameters for ABAQUS. *Jurnal Ilmu Pendidikan*, 7(2), 809-820.

Ellobody, E, Young B, Lam D (2006). Behaviour of normal and high strength concrete-filled compact steel tube circular stub columns. *Journal of Constructional Steel Research,* 62(7), 706-715.

Feng Z, Wang X, Zhang S, Chu Y (2022). Experimental investigation on cantilever square CFST columns under lateral continuous impact loads. *Journal of Constructional Steel Research*, 196(2), 107416.

Giakoumelis G, Lam D (2004). Axial capacity of circular concrete-filled tube columns*. Journal of Constructional Steel Research,* 60(7), 1049-1068.

Guler S, Lale E, Aydogan M (2013). Behaviour of SFRC filled steel tube columns under axial load. *Journal of Advanced Steel Construction*, 9(1), 14-25.

Hassam M, Guo LH, Wang YH (2020). Experimental and numerical investigation of cross-shaped stub CFSTs under axial compression. *Magazine of Concrete Research*, 73(23), 1225-1240.

Hassam M, Geo LH, Chen J (2022). Concentric and eccentric compression performance of multiple-cell cruciform CFSTs. *Journal of Constructional Steel Research*, 192(3), 107205.

Hou CC, Han LH (2018). Life-cycle performance of deteriorated concrete-filled steel tubular (CFST) structures subject to lateral impact. *Thin-Walled Structures*, 132(11), 362-374.

Hu HT, Schnobrich WC (1989). Constitutive modeling of concrete by using nonassociated plasticity*. Journal of Materials in Civil Engineering*, 1(4), 199–216.

Hu HT, Huang CS, Wu MH, Wu YM (2003). Nonlinear analysis of axially loaded concrete-filled tube columns with confinement effect. *Journal of Structural Engineering ASCE,* 129(10), 1322–1329.

ISO 1920-3:2004 (2004). Testing of concrete – Part 3: Making and curing test specimens. International Organization for Standardization, Geneva, Switzerland.

Kirankumar P, Babu S, Ram D (2016). Comparative study of concrete filled steel tube columns under axial compression. *International Journal of Constructive Research in Civil Engineering*, 2(2), 11-17.

Krolak M, Kowal-Michalska K, Mania R, Swiniarski, J (2007). Experimental tests of stability and load carrying capacity of compressed thin-walled multi-cell columns of triangular cross-section. *Thin-Walled Structures*, 45(10), 883-887.

Królak M, Mechalska K, Mania R, Swiniarski J (2009). Stability and load-carrying capacity of multi-cell thin-walled columns of rectangular cross-sections. *Journal of Theoretical and Applied Mechanics*, 47(2), 435-456.

Mander JB, Priestley MJN, Park R (1988). Theoretical stress–strain model for confined concrete*. Journal Structural Engineering,* 114(8), 1804-1826.

Patil B, Mohite P (2014). Parametric study of square concrete filled steel tube columns subjected to concentric loading. *International Journal of Engineering Research and Applications*, 4(8), 109-112.

Richart FE, Brandtzaeg A, Brown RL (1928). A study of the failure of concrete under combined compressive stresses. *Bulletin 185, Univ. of Illinois Engineering Experimental Station*, Champaign, 111.

Saenz LP (1964). Discussion of 'Equation for the stress–strain curve of concrete' by Desayi P. Krishnan S*. Journal of American Concrete Institute*, 61, 1229–1235.

Seangatith S (1997). Characterization and analysis of composite beams subjected to impact loads. *Ph.D. thesis*, University of Texas at Arlington, Arlington, TX, USA.

Sofi M (2015). A review on energy absorption of multi cell thin walled structure*. Journal of Advanced Review on Scientific Research*, 16(1), 18-24.

Song J, Chen Y, Lu G (2012). Axial crushing of thin-walled structures with origami patterns. *Thin-Walled Structures*, 54, 65–71.

Tran T, Hou S, Han X, Chau M (2015). Crushing analysis and numerical optimization of angle element structures under axial impact loading. *Composite Structures*, 119, 422–435.

Tran T, Hou S, Han X, Nguyen N, Chau M (2014). Theoretical prediction and crashworthiness optimization of multi-cell square tubes under oblique impact loading. *International Journal of Mechanical Sciences*, 89, 177–193.

Uslu F, Taşkın K (2024). Experimental and Finite element method investigation of axial load carrying capacity of concrete filled circular steel tube columns according to different slenderness ratios. *International Journal of Steel Structures*, 24(3), 619–634.

Wardenier J (2001). Hollow sections in structural applications. Edited by CIDECT-Comité International pour le Développement et l'Etude de la Construction Tubulaire, John Wiley & Sons, Australia.

Wardenier J, Packer J, Zhao X-L, van der Vegte G (2010). Hollow sections in structural applications. 2nd edition, Edited by CIDECT - Comité International pour le Développement et l'Etude de la Construction Tubulaire. Bouwen met staal, Zeotemeer, Netherlands.

Wu S, Zheng G, Sun G, Liu Q, Li G, Li Q (2016). On design of multi-cell thin-wall structures for crashworthiness. *International Journal of Impact Engineering*, 88, 102–117.

Yang X, Yang H, Zhang S (2019). Rate-dependent constitutive models of S690 high- strength structural steel. *Construction and Building Materials*, 198(7), 597–607.

Yang H, Zhang JC, Du GF, Mao ZH (2021). Experimental study on the behavior of cross-shaped concrete-filled steel tubular intermediate long columns under axial compression. *Progress in Steel Building Structures*, 23(7), 49-57.

Yin H, Wen G, Liu Z, Qing Q (2014). Crashworthiness optimization design for foam-filled multi-cell thin-walled structures. *Thin-Walled Structures*, 75, 8–17.

Yin H, Xiao Y, Wen G, Qing Q, Deng Y (2015). Multiobjective optimization for foam-filled multi-cell thin-walled structures under lateral impact. *Thin-Walled Structures*, 94, 1–12.

Yousuf M, Uy B, Tao Z (2010). Experimental behaviour of pre-compressed concrete-filled stainless steel tubular columns subjected to transverse impact loads. *4th International Conference on Steel & Composite Structure*, 21-23 July 2010, Sydney, Australia.

Yousuf M, UY B, Tao Z, Remennikov A, Liew R (2012). Behaviour and resistance of hollow and concrete-filled mild steel columns due to transverse impact loading. *Australian Journal of Structural Engineering*, 13(1), 65-80.

Zhang X, Cheng G, Zhang H (2006). Theoretical prediction and numerical simulation of multi-cell square thin-walled structures. *Thin-Walled Structures*, 44(11), 1185–1191.

Zheng Y, Lin Y, Ma S (2024). Axial compressive behavior of stiffened and multi-cell cross-shaped CFST stub columns. *Constructional Steel Research*, 213, 108399.

Zhu A-Z, Xu W, Gao K, Ge H-B, Zhu J-H (2018). Lateral impact response of rectangular hollow and partially concrete-filled steel tubular columns. *Thin-Walled Structures*, 130(9), 114-131.

Zhu Y, Gardner L, Yang H (2023). Experimental investigation into the transverse impact performance of high-strength circular CFST members*. Thin-Walled Structures,* 189(3), 110923.